

Properties of a Supercritical Quasi-perpendicular Interplanetary Shock Propagating in the Terrestrial Foreshock Region

Mingzhe Liu, Zhongwei Yang, Ying D. Liu, Bertrand Lembège, Karine Issautier, L. B. Wilson III, Siqi Zhao, Vamsee Krishna Jagarlamudi, Xiaowei Zhao, Jia Huang, et al.

▶ **To cite this version:**

Mingzhe Liu, Zhongwei Yang, Ying D. Liu, Bertrand Lembège, Karine Issautier, et al.. Properties of a Supercritical Quasi-perpendicular Interplanetary Shock Propagating in the Terrestrial Foreshock Region. The Astrophysical Journal Supplement Series, 2022, 263 (November), 11 (15p.). 10.3847/1538-4365/ac94c8 . insu-03849861

HAL Id: insu-03849861

https://insu.hal.science/insu-03849861

Submitted on 12 Nov 2022

HAL is a multi-disciplinary open access archive for the deposit and dissemination of scientific research documents, whether they are published or not. The documents may come from teaching and research institutions in France or abroad, or from public or private research centers.

L'archive ouverte pluridisciplinaire **HAL**, est destinée au dépôt et à la diffusion de documents scientifiques de niveau recherche, publiés ou non, émanant des établissements d'enseignement et de recherche français ou étrangers, des laboratoires publics ou privés.



Distributed under a Creative Commons Attribution - NonCommercial 4.0 International License

The Astrophysical Journal Supplement Series, 263:11 (15pp), 2022 November https://doi.org/10.3847/1538-4365/ac94c8
© 2022. The Author(s). Published by the American Astronomical Society.
OPEN ACCESS

Properties of a Supercritical Quasi-perpendicular Interplanetary Shock Propagating in the Terrestrial Foreshock Region

Mingzhe Liu[1,2,3], Zhongwei Yang[2,4], Ying D. Liu[2,4], Bertrand Lembège[3], Karine Issautier[1], L. B. Wilson, III[5], Siqi Zhao[6], Vamsee Krishna Jagarlamudi[7], Xiaowei Zhao[8,9], Jia Huang[10], and Nicolina Chrysaphi[1]
[1] LESIA, Observatoire de Paris, Université PSL, CNRS, Sorbonne Université, Université de Paris, 5 place Jules Janssen, F-92195 Meudon, France
mingzhe.liu@obspm.fr
[2] State Key Laboratory of Space Weather, National Space Science Center, Chinese Academy of Sciences, Beijing 100190, People's Republic of China
[3] LATMOS / IPSL, UVSQ Paris-Saclay University, Sorbonne University, CNRS, Guyancourt, France
[4] University of Chinese Academy of Sciences, Beijing 100049, People's Republic of China
[5] NASA Goddard Space Flight Center, Code 672, Greenbelt, Maryland, MD20707, USA
[6] Deutsches Elektronen Synchrotron, Platanenallee 6, D-15738 Zeuthen, Germany
[7] Johns Hopkins University Applied Physics Laboratory, Laurel, MD, USA
[8] Key Laboratory of Space Weather, National Satellite Meteorological Center (National Center for Space Weather), China Meteorological Administration, Beijing 100081, People's Republic of China
[9] School of Earth and Space Sciences, Peking University, Beijing 100871, People's Republic of China
[10] Climate and Space Sciences and Engineering, University of Michigan, Ann Arbor, MI 48109, USA
Received 2022 May 11; revised 2022 September 6; accepted 2022 September 22; published 2022 November 9

Abstract

We investigate the properties of an interplanetary (IP) shock ($M_f = 2.1$, $\theta = 80°$) that was detected by Wind on 1999 September 12 and was magnetically connected to the terrestrial bow shock. Key results are obtained concerning how the IP shock modifies the terrestrial foreshock electron and ion dynamics: (1) Intensive Langmuir waves were detected downstream of the IP shock due to the enhanced penetrating terrestrial foreshock electron beams. (2) Whistler heat flux instabilities associated with the oblique precursor whistler pitch-angle scatter the suprathermal electrons, together with the normal betatron acceleration that occurs across the IP shock. (3) The IP shock interacts with the antisunward propagating Alfvén waves/fluctuations, and the shocked plasma shows both Alfvénic and mirror-mode features where Alfvén waves were separated into two parts propagating in opposite directions. (4) Intense specularly reflected gyrating ions were detected around the IP shock, which indicates that the energy dissipation effects at the IP shock depend on both reflected ions and the waves intrinsic to the shock. These results provide new insights into the interaction between an IP shock and the terrestrial foreshock.

Unified Astronomy Thesaurus concepts: Solar wind (1534); Interplanetary shocks (829); Alfven waves (23); Shocks (2086); Planetary bow shocks (1246)

1. Introduction

Collisionless shocks are important plasma structures, and appear ubiquitously in the solar wind and around the planets. From the Sun to the Earth, interplanetary (IP) shocks are typically driven by coronal mass ejections (CMEs) or by the fast solar wind (e.g., Liu et al. 2012, 2014a, 2014b; Möstl et al. 2012; Lugaz et al. 2015; Zhao et al. 2019b). Near the Earth, the bow shock forms in front of the Earth due to the interaction between the solar wind and the Earth's magnetosphere. Upstream of the terrestrial bow shock, the region that is magnetically connected to the shock is called the terrestrial foreshock. It is well-known and has long been investigated that the terrestrial foreshock region is dominated by waves and backstreaming particles (Wilson 2016; Parks et al. 2017). When IP shocks are Earth directed, they may interact with the terrestrial foreshock region, which is of great significance for both space weather predictions and fundamental plasma physics (e.g., Přech et al. 2009; Šafránková et al. 2007a, 2007b; Goncharov et al. 2018). Previous studies mainly focused on how the mutual interaction modifies the geometry, propagation, and strength of the IP shock. There are still very few studies of how an IP shock modifies terrestrial foreshock electron and ion dynamics and associated waves, however.

Terrestrial foreshocks are identified by the enhanced flux of backstreaming particles. Due to the $\boldsymbol{E} \times \boldsymbol{B}$ drift and high mass ratio between the ions and electrons, a clear separation appears between the ion and electron foreshock boundaries (see Parks et al. 2017). In the region between the ion and electron foreshock boundaries, only backstreaming electrons are detected. In contrast, in the ion foreshock region, both backstreaming ions and electrons are observed. The backstreaming electrons can exhibit a bump on tail electron velocity distribution function that is unstable to the growth of Langmuir waves via Landau resonance (see Savoini & Lembège 2001; Pulupa et al. 2011, 2012, and references therein). Savoini & Lembège (2001) showed that local backstreaming-electron distributions consist of two components: (i) a high-energy component characterized by a field-aligned bump on tail or beam signature, and/or (ii) a low-energy component characterized by a loss-cone signature. Also, electrons that are locally accelerated in the deep downstream region may escape back into the upstream region (Savoini & Lembege 2009). Furthermore, in the leading edge of the electron foreshock region, the most intense Langmuir waves around the local electron plasma frequency (f_{pe}) are generally observed, associated with more energetic backstreaming-electron beams above 1 keV (e.g., Kasaba et al. 2000; Bale et al. 2000; Pulupa et al. 2012). In addition, in the deeper region of the

Original content from this work may be used under the terms of the Creative Commons Attribution 4.0 licence. Any further distribution of this work must maintain attribution to the author(s) and the title of the work, journal citation and DOI.

terrestrial foreshock, weaker Langmuir waves are detected in association with less energetic backstreaming electrons below 1 keV (e.g., Matsumoto et al. 1997; Kasaba et al. 2000; Pulupa et al. 2011). The $2f_{pe}$ emissions, frequently detected in the terrestrial foreshock, are considered to be generated by backstreaming-electron-driven Langmuir waves and correlated with the amplitude of Langmuir waves. Then, the $2f_{pe}$ emission source region is confirmed to be the leading region of the electron foreshock (e.g., Yoon et al. 1994; Reiner et al. 1996; Kasaba et al. 2000). Above all, when backstreaming electrons and associated electrostatic Langmuir waves/fluctuations are detected upstream of the terrestrial bow shock, the spacecraft is considered to be magnetically connected to the terrestrial bow shock. Thus, an interesting question arises regarding how an IP shock modifies the terrestrial foreshock electron dynamics when the IP shock is magnetically connected to the terrestrial bow shock.

The backstreaming ions near the ion foreshock boundary are field aligned and become more diffuse and isotropic when they travel deeper into the foreshock and/or approach the quasi-parallel shock region (Wilson 2016). Due to the interaction between the incoming and backstreaming ions, numerous large-amplitude waves/fluctuations that fall in a broad frequency range were detected in the quasi-parallel foreshock region (e.g., low-frequency Alfvén/ion cyclotron waves, and fast magnetosonic or magnetosonic-whistler waves). Alfvén waves and/or Alfvén-like oscillations were frequently detected in the quasi-parallel terrestrial foreshock region in association with the left-hand resonant ion/ion instability (e.g., Wang et al. 2015; Wilson 2016, and references therein). In particular, when a quasi-perpendicular IP shock is Earth directed, it may interact with Alfvén waves/fluctuations in the quasi-parallel terrestrial foreshock. In the past, many theoretical and simulation investigations focused on the interaction of Alfvén waves with shocks (e.g., McKenzie & Westphal 1969; Lu et al. 2009). The amplitude of the Alfvén waves is enhanced by the shock (e.g., McKenzie & Westphal 1969; Lu et al. 2009), and Alfvén waves detected in the shocked plasma are separated into two branches propagating in the opposite directions (Lu et al. 2009). Furthermore, clear ripples were identified at the front of the perpendicular shock due to the interaction with the upstream Alfvén waves based on two-dimensional hybrid simulations (Lu et al. 2009). The ripples at the shock front can affect both reflected ion and electron dynamics (e.g., Lembège & Savoini 2002; Lembege et al. 2004; Saito & Umeda 2011; Yang et al. 2012, 2018). Interactions between the Alfvén waves/fluctuations and a quasi-perpendicular shock are still an interesting issue that is far from completely understood. Examination of the features of the particle populations and waves around the IP shock interacting with Alfvén waves/fluctuations may provide new insights.

In this work, we report properties of an IP shock propagating in the quasi-parallel terrestrial foreshock region, which was observed by Wind (Wilson et al. 2021) at 03:57:56 UT on 1999 September 12. Specifically, in situ measurements of the solar wind from Wind/MFI (Lepping et al. 1995), Wind/3DP (Lin et al. 1995) and the thermal noise receiver (TNR) on board Wind/WAVES (Bougeret et al. 1995) have been used for the analysis. In Section 2.1, we confirm that the IP shock is magnetically connected to the terrestrial bow shock via a comprehensive analysis of magnetic field measurements, electron pitch-angle distributions (PADs), and wave observations. Then, with high-cadence magnetic field data (11 samples per second) and the burst-mode particle data (a full distribution per three seconds), we investigate how the IP shock modifies the electron dynamics of the terrestrial foreshock at kinetic scales in Section 2.2. Furthermore, the interactions between the IP shock and the Alfvén waves/fluctuations detected in the terrestrial foreshock region are reported in Section 2.3, including the properties of Alfvén waves/fluctuations around the IP shock and the IP shock-reflected ion dynamics. In the end, the main results are summarized and discussed in Section 3.

2. Observations and Data Analysis

2.1. Magnetic Connection between IP Shock and Terrestrial Bow Shock

Figure 1 (left) shows the Wind spacecraft trajectory (solid black curve) projected in the *XY*-GSE plane, which covers the time period from 00:00:00 on 1999 September 10, UTC, to 12:00:00 on 1999 September 12, UTC. Projections of the model terrestrial bow shock (solid red curve; see Peredo et al. 1995) and magnetopause (solid blue curve; see Roelof & Sibeck 1993) locations are also plotted for reference. The model bow shock parameters are adjusted to match the average location of the observed crossings by the spacecraft. During the time period considered, the spacecraft traveled across the quasi-parallel side of the terrestrial bow shock from the downstream (magnetosheath) to the upstream and then detected an IP shock (yellow asterisk). The projection of the average magnetic field vector was determined by averaging the magnetic field during the time period between the last crossing of the terrestrial bow shock and detection of the IP shock. As a result, Wind may generally be magnetically connected to the terrestrial bow shock along the trajectory between the terrestrial bow shock and the IP shock. For the basic information of the IP shock, it passed the Wind spacecraft at 03:57:56 UT on 1999 September 12. The IP shock that is in the supercritical regime with a fast magnetosonic Mach number $M_f \sim 2.1$ and an Alfvén Mach number $M_A \sim 3.0$ propagates in the proton plasma beta $\beta_p \approx 1$ environment. It is a fast-mode, quasi-perpendicular shock, with a shock normal angle $\theta_{Bn} = 80^\circ$ and a shock speed $V_{shn} = 532.8 \pm 3.3\ \mathrm{km\ s^{-1}}$. The basic parameters of the IP shock are obtained by the shock discontinuity analysis tool (Vinas & Scudder 1986). They are consistent with those from the shock database maintained by J. C. Kasper.[11]

Figure 1 (right) presents an overview plot of the Wind observations along the spacecraft trajectory mentioned above. Figures 1(b)–(c) give the magnetic field magnitude and GSE components of the magnetic field, respectively. From the terrestrial bow shock (dashed vertical red line) to the IP shock (dashed vertical yellow line), the magnetic field magnitude decreases in general. Furthermore, the X-GSE component (in red) of the magnetic field is positive in general ($<B_x> \sim 2.1$ nT) and the Y-GSE component (in green) of the magnetic field is usually negative ($<B_y> \sim -3.0$ nT). This implies that the observed ambient magnetic field is generally directed sunward. Therefore, electrons with pitch angles close to 0° are traveling toward the Sun and may be backstreaming from the bow shock. In contrast, electrons with pitch angles close to 180° are traveling antisunward and may be incident to the bow shock. Figure 1(d) presents the PAD of 265 eV electrons measured by EESA-Low/

[11] https://www.cfa.harvard.edu/shocks/

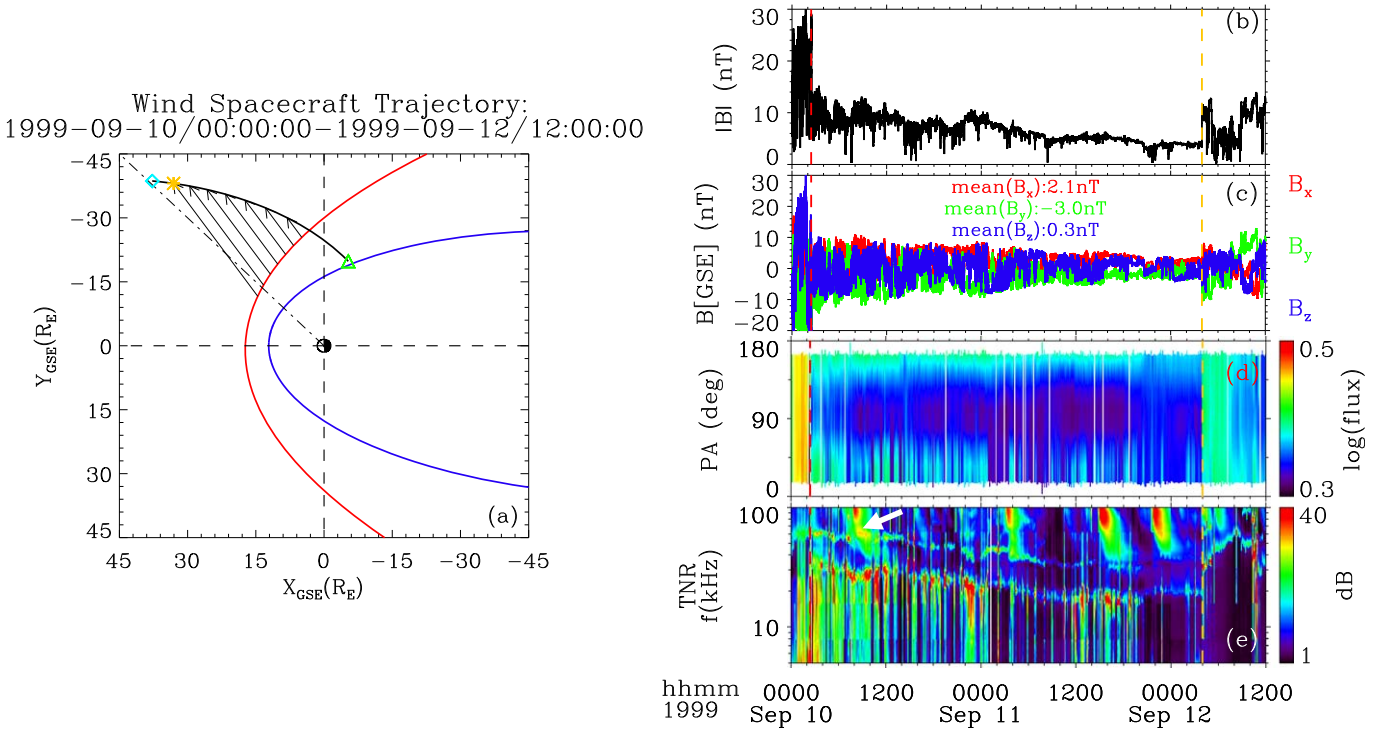


Figure 1. (Left) The Wind satellite orbits in the *XY* plane of geocentric solar ecliptic (GSE) coordinate reference frame from 00:00:00 on 1999 September 10, UTC, to 12:00:00 on 1999 September 12, UTC. The solid black line denotes the spacecraft trajectory. The empirical model bow shock (solid red line; see Peredo et al. 1995) and magnetopause (solid blue line; see Roelof & Sibeck 1993) are plotted for reference. The triangle and diamond mark the start and end of the Wind trajectory, respectively. The asterisk denotes the position where an IP shock was detected by Wind. The black arrows represents the projection of the average magnetic field vectors between the terrestrial bow shock and the IP shock. (Right) The Wind observations that correspond to the trajectory shown on the left. From top to bottom, the panels show the magnetic field magnitude, magnetic field components in GSE coordinates, the PAD of 265 eV electrons obtained from the EESA-Low instrument on board Wind/3DP, and the electric field voltage dynamic spectrum from TNR on board Wind/WAVES. The dashed vertical red and yellow lines mark the crossing of the terrestrial bow shock and the IP shock, respectively.

3DP for reference. Typically, the relevant electron populations of this energy are the halo and/or strahl in the quiet solar wind or bidirectional streams of suprathermal electrons within CMEs (Gosling et al. 1987). Here, the strahl electrons from the Sun are apparent in the direction antiparallel to the magnetic field, whereas terrestrial foreshock electron beams (backstreaming electrons from the bow shock) are clearly identified as evident enhancements when pitch angles are smaller than 90°. Figure 1(e) shows the electric field voltage dynamic spectrum measured by TNR on board Wind/WAVES. The TNR radio receiver on board Wind/WAVES, which is connected to the 2×50 m thin wire electric dipole antennas (before it was broken by dust impacts), measures electric fields (from 4 to 256 kHz) by combining five logarithmically spaced (overlapping) frequency bands (with the standard frequency resolution being $\Delta f/f = 4.3\%$). The TNR radio receiver is especially designed to measure electrostatic fluctuations produced by the quasi-thermal noise due to the thermal motion of the ambient electrons and ions. The quasi-thermal plasma line is clearly visible (between 20 and 40 kHz before and after the IP shock) and can be used to straightforwardly determine the local electron density (e.g., Meyer-Vernet & Perche 1989; Meyer-Vernet et al. 2017). The Langmuir wave activity can be identified as the intense enhancement near the plasma line. As expected, intense Langmuir waves are associated with transient enhancements of the electron flux in parallel direction. Also, $2f_{pe}$ emissions are clearly detected during the time period considered. Again, observations of the terrestrial foreshock electron beams along the magnetic field and the associated Langmuir wave activity indicate that Wind may in general be magnetically connected to the terrestrial bow shock along the trajectory between the terrestrial bow shock and the IP shock. In addition, the timespan of the electron foreshock region of a quasi-perpendicular IP shock observed by the spacecraft is usually shorter than one minute (e.g., Bale et al. 1999; Hoang et al. 2007; Pulupa & Bale 2008). Therefore, we exclude the possibility that the terrestrial foreshock electrons and strahl electrons are disturbed by the IP foreshock electrons. More details are described in Appendices A and B.

We note that the terrestrial foreshock electron beams are observed intermittently, whereas the strahl electrons from the Sun are observed constantly. This may be due to the dynamic nature of the terrestrial bow shock, especially the large-scale bow shock expansion (i.e., back and forth movements) due to the solar wind compression. For the time period considered, Wind crossed the bow shock three times due to the expansion from 02:00:00 to 03:00:00 on 1999 September 10, UTC. In addition, the ambient magnetic field rotates slightly. As a result, it may connect to different regions on the bow shock and/or disconnect to the bow shock. In contrast, in Figure 1(a), both the model bow shock and the projected upstream magnetic field lines are assumed to be static. Therefore, Wind may not always be magnetically connected to the bow shock (although it was for most of the time considered), which may be the main reason for the intermittent features of the terrestrial foreshock electron beams. Furthermore, when Wind is magnetically connected to the quasi-perpendicular terrestrial bow shock, Lembège & Savoini (2002) showed that electrons may not be reflected uniformly by the bow shock based on two-

dimensional full particle electromagnetic simulation. Instead, packs of reflected electrons may be formed along the rippled shock front. This may also contribute to the intermittent features of the terrestrial foreshock electron beams. Also, a few weak Type III radio bursts were observed with a cutoff frequency much higher than local f_{pe} (except for the one indicated by the white arrow in Figure 1(e)). This indicates that most Langmuir waves detected between the terrestrial bow shock and the IP shock are not associated with the energetic electrons from the Sun, but are driven by the terrestrial foreshock electron beams.

An expanded view of 5 hr observations around the IP shock (indicated by the vertical red line) is shown in Figure 2. The plasma line is apparent, and both local f_{pe} and $2f_{pe}$ are overplotted as white dots in Figure 2(a) for reference. Accurate measurements of local f_{pe} are derived by tracking the plasma peaks based on the neural network method, whose accuracy is verified by the full fit of the quasi-thermal noise spectrum (see Salem et al. 2001; Issautier et al. 2005, and references therein). Moreover, Figures 2(b)–(e) show that the transient electron flux enhancements around the IP shock mainly come from the direction parallel to the ambient magnetic field. More details about the detectors and specific definition of the directions are given in Appendix A. Thereby, we verified that the transient parallel electron flux enhancements exclusively come from the terrestrial bow shock and therefore correspond to the terrestrial foreshock electrons. Indeed, intermittent Langmuir waves (Figure 2(a)) driven by transient terrestrial foreshock electron beams are observed around the IP shock. We note that a weak Type III burst was observed around the IP shock. The cutoff frequency of the Type III burst is much higher than local f_{pe}, which means that the corresponding flare-accelerated energetic electrons did not reach the spacecraft. We further checked the EESA-High/3DP ($\sim$300 eV $\leqslant E \leqslant$ 30 keV) and SST-Foil/3DP ($\sim$20 keV $\leqslant E \leqslant$ 500 keV) measurements and indeed found no apparent enhancements of the antisunward energetic electron flux (not shown here). Therefore, we confirm that the Langmuir waves detected around the IP shock were exclusively driven by the terrestrial foreshock electrons and not associated with the energetic electrons from the Sun. Thus, it is quite striking to mention that the intensity of the bursty Langmuir waves detected downstream of the IP shock is much higher than those upstream of the IP shock. Figures 2(a) and (f) show that the detected Langmuir wave intensity is closely related to the ratio of the parallel to perpendicular electron flux. When the terrestrial foreshock electrons and the associated Langmuir waves are detected, the ratio of the parallel to the perpendicular electron flux is higher than the ambient values in the free solar wind. Upstream of the IP shock, the ratio of the parallel to the perpendicular electron flux is highest for the terrestrial foreshock electrons with an energy from 96 to 258 eV (see the green lines in Figure 2(f)). In contrast, downstream of the IP shock, the energy of the dominant terrestrial foreshock electrons (with a higher ratio of the parallel to perpendicular electron flux) is higher than 420 eV (see the dark blue and/or purple lines in Figure 2(f)). Across the IP shock, the energy of the dominant terrestrial foreshock electrons and the corresponding ratio of the parallel to perpendicular electron flux are greatly enhanced. This coincides with the enhanced Langmuir wave activity downstream of the IP shock. The possible driving mechanisms are explained in Section 2.2.

2.2. Electron Dynamics at Kinetic Scales

In this section, we investigate how the electron features are modified across the IP shock at kinetic scales, which are associated with the mechanisms of wave generations/enhancements. Full electron PADs around the IP shock are plotted in Figure 3. The labeled energies in Figure 3 are the mean values of the nine highest energy channels of EESA-Low/3DP after correcting the estimated spacecraft potential (Salem et al. 2001). Figures 3(a)–(b) present the observations upstream of the IP shock. Figure 3(c) covers the foot, ramp, and overshoot structures of the IP shock. Figures 3(d)–(f) give the observations downstream of the IP shock. The foot, ramp, and overshoot structures are clearly displayed in both Figures 4(a) and 7 (a). In Figures 3(a)–(b), both the electron (with an energy higher than 35 eV) number flux and the energy flux along the magnetic field (including both parallel, PA $< 45°$, and antiparallel, PA $> 135°$) are higher than those perpendicular (PA $= 90°$) to the magnetic field. We confirm that IP foreshock electrons were not detected by Wind in Appendix B. Therefore, suprathermal electrons flowing parallel (antiparallel) to the ambient magnetic field correspond to the terrestrial foreshock electron beams (strahl electrons from the Sun). This gives further confirmation that the IP shock is indeed magnetically connected to the terrestrial bow shock.

We note that both the suprathermal electron number flux and the energy flux perpendicular to the ambient magnetic field (i.e., PA $= 90°$) increase from upstream to the shock ramp position (see Figures 3 (a)–(c)). This enhancement may be explained by the pitch-angle scattering by the whistler heat flux instabilities observed near the shock ramp, together with the normal betatron acceleration of electrons (see below). Downstream of the IP shock, the parallel suprathermal (especially with an energy higher than 258 eV) electron flux (PA $< 45°$) is in general higher than those antiparallel (PA $> 135°$) and perpendicular (PA $= 90°$) to the ambient magnetic field. This is consistent with the enhanced ratio of the parallel to perpendicular suprathermal electron flux across the IP shock mentioned in Section 2.1 (see Figure 2(f)). This may account for the generation and/or enhancement of intensive Langmuir wave activity downstream of the IP shock. When the transient terrestrial foreshock electrons penetrate the IP shock, the parallel terrestrial foreshock electron flux is enhanced accordingly. Stated in another way, the transient electron flux enhancements upstream of the IP shock are further enhanced when penetrating the IP shock (e.g., Figure 2). Downstream of the IP shock, the further enhanced terrestrial foreshock electron beams may contribute to create a larger bump on tail distributions. In Figure 2(f), the higher energy parallel electron fluxes can sometimes reach the lower energy parallel fluxes (higher than 258 eV) when terrestrial foreshock electrons are detected, which may be remnants of positive slopes. Indeed, even though the parallel electron fluxes at higher energies are enhanced (see both Figures 2(f) and 3), they are not high enough to produce positive slopes on the tail of the electron distributions. There are two possible explanations: (i) the bump (the region with a positive slope) on the tail of the distribution function has already been relaxed to generate and/or enhance the Langmuir waves, or (ii) the bump still exists, but the EESA instruments on board Wind/3DP have an insufficient energy resolution to resolve it. Based on the quasilinear theory of beam relaxation (e.g., Grognard 1975; Pulupa et al. 2012; Zhao et al. 2021b, and references therein), positive slopes on the bump on

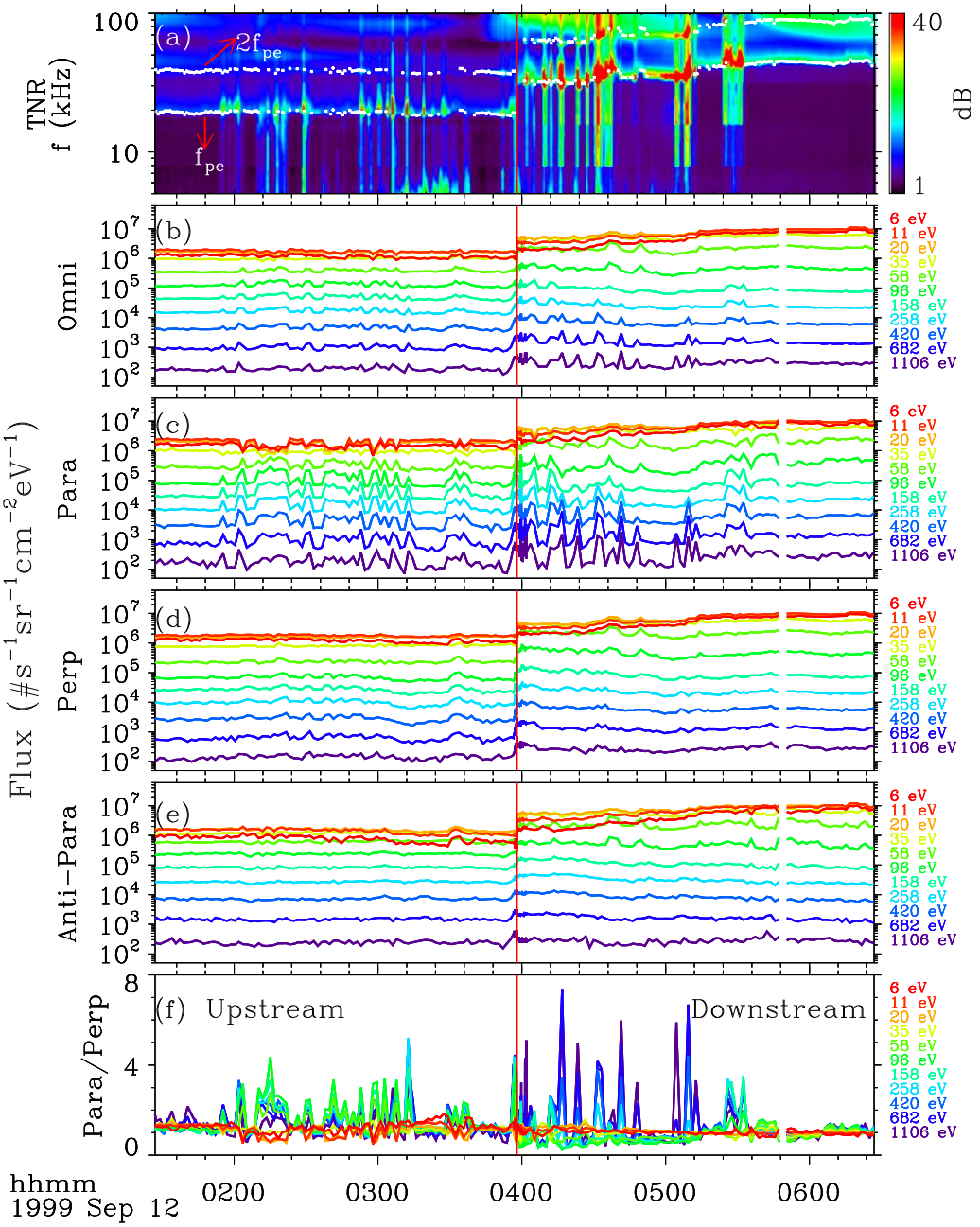
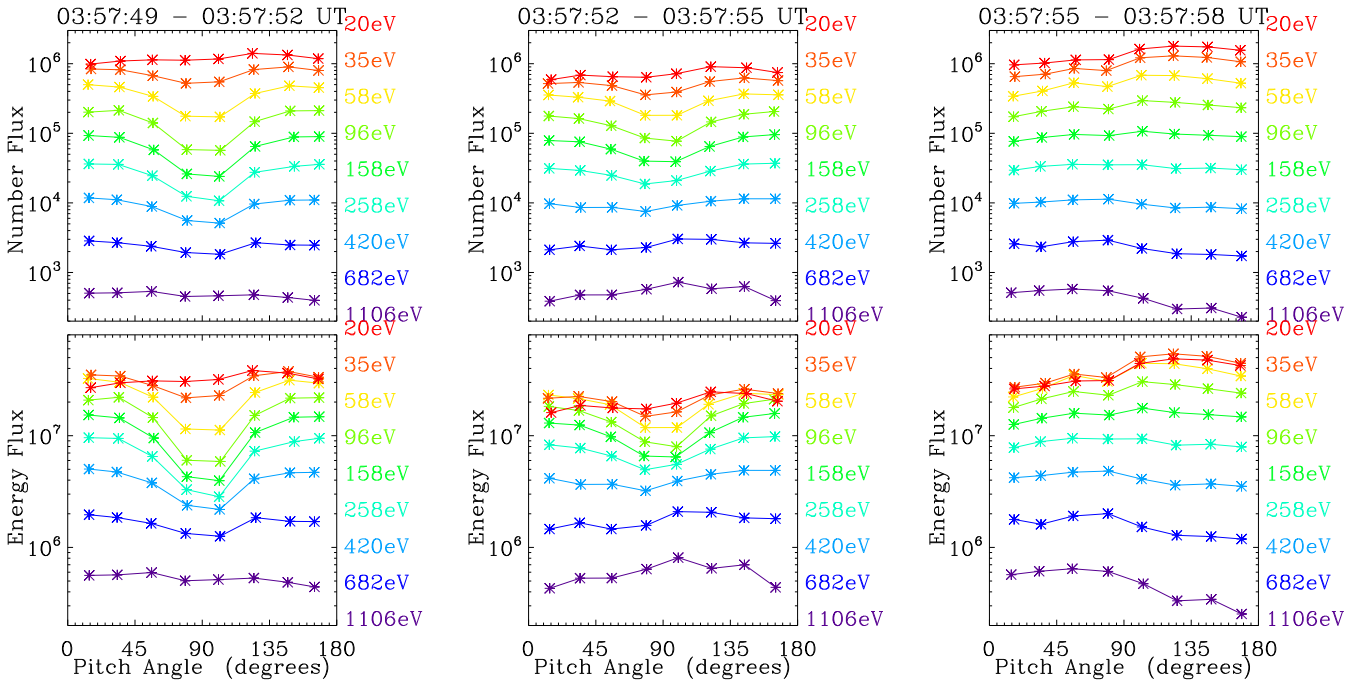


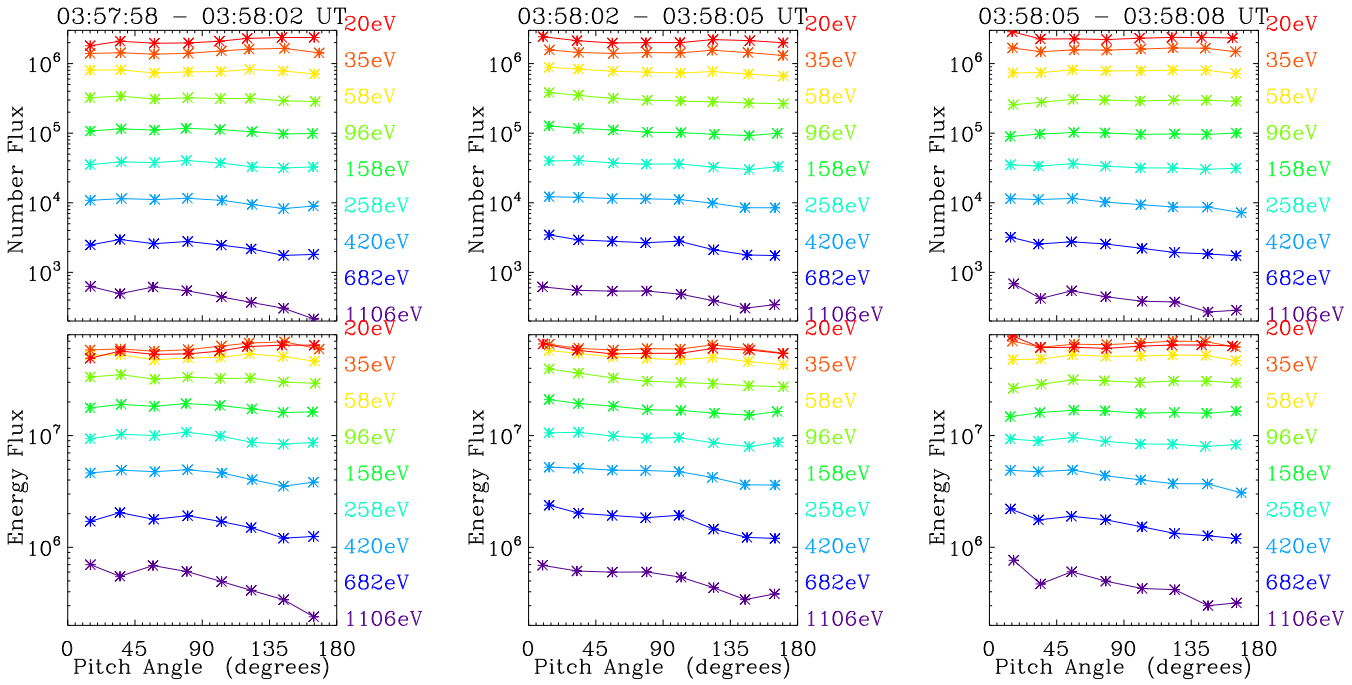
Figure 2. Five-hour expanded view of measurements from Wind around the IP shock detected at 03:57:56 on 1999 September 12, UT. From top to bottom, the panels show the electron field voltage power spectrum from TNR on board Wind/WAVES, omnidirectional electron flux, electron flux at different pitch angles including those parallel, perpendicular, and antiparallel to the ambient magnetic field, and the ratio of the parallel to perpendicular flux. For electron fluxes at different pitch angles, they are derived from the measurements by the EESA-Low instrument on board Wind/3DP, and electrons from about 6 to 1106 eV are considered. The labeled energies have been corrected by considering the spacecraft potential. The vertical red line marks the time when the IP shock was detected.

tail electron velocity distributions can be mediated by Landau resonance and then further generate/enhance Langmuir waves. The intensity of the Langmuir waves depends on both the energy of the electron beam and the height of the bump on tail distribution, which could explain the more intensive Langmuir waves downstream of the IP shock well.

Figure 4 gives the wavelet analysis of the magnetic field at a high cadence of 11 samples s^{-1} around the IP shock with a 2-minute time interval considered. The magnetic foot associated with the precursor whistlers and the magnetic overshoot are indicated by two arrows in Figure 4(a), respectively. A detailed view of the magnetic foot and overshoot is shown in Figure 7(a). Across the IP shock, the magnetic field magnitude is enhanced. This field jump (at the foot and ramp of the shock) lasts for about 5 s, much longer than the electron cyclotron period T_{ce} (0.0038 s $< T_{ce} <$ 0.0086 s). Therefore, the first adiabatic invariant $\mu = E_{\perp}/B$ should be conserved during the compression, which means that normal betatron acceleration of electrons may exist. Normal betatron acceleration of electrons mainly occurs before and at the IP shock (at the foot and ramp of the shock), as the variation of the magnetic field magnitude almost remains relatively small downstream of the IP shock. The normal betatron acceleration of electrons may contribute to the change of the pitch angle of electrons (Liu et al. 2018).



(a) upstream (b) upstream (c) foot+ramp+overshoot



(d) downstream (e) downstream (f) downstream

Figure 3. Evolution of the stacked line plot of the PADs at the nine highest energies (after correcting the spacecraft potential) from the EESA-Low instrument on board Wind/3DP. The top/bottom panel of each figure shows the electron PAD of number/energy flux. The physics units are the number flux ($\#s^{-1}sr^{-1}cm^{-2}eV^{-1}$) and the energy flux ($eVs^{-1}sr^{-1}cm^{-2}eV^{-1}$).

Precursor whistlers (indicated by the white arrows in Figures 4(c)–(f)) are observed at $2.0\,\mathrm{Hz} < f < 4.0\,\mathrm{Hz}$ (in spacecraft frame) near the shock ramp. Figure 5 shows an example of a minimum variance (MV) analysis (Khrabrov & Sonnerup 1998) of the magnetic fluctuations at $2.0\,\mathrm{Hz} < f < 4.0\,\mathrm{Hz}$ (in spacecraft frame) at the foot/precursor region of the IP shock. The hodograms in GSE and MV coordinates are shown in the left and right panels, respectively. The wave event is right-handed polarized with respect to the local magnetic field, which is consistent with the whistler properties. The wave event is also right-handed polarized with respect to the wavevector $\hat{K}_{\mathrm{GSE}}$. However, there is an ambiguity of the sign

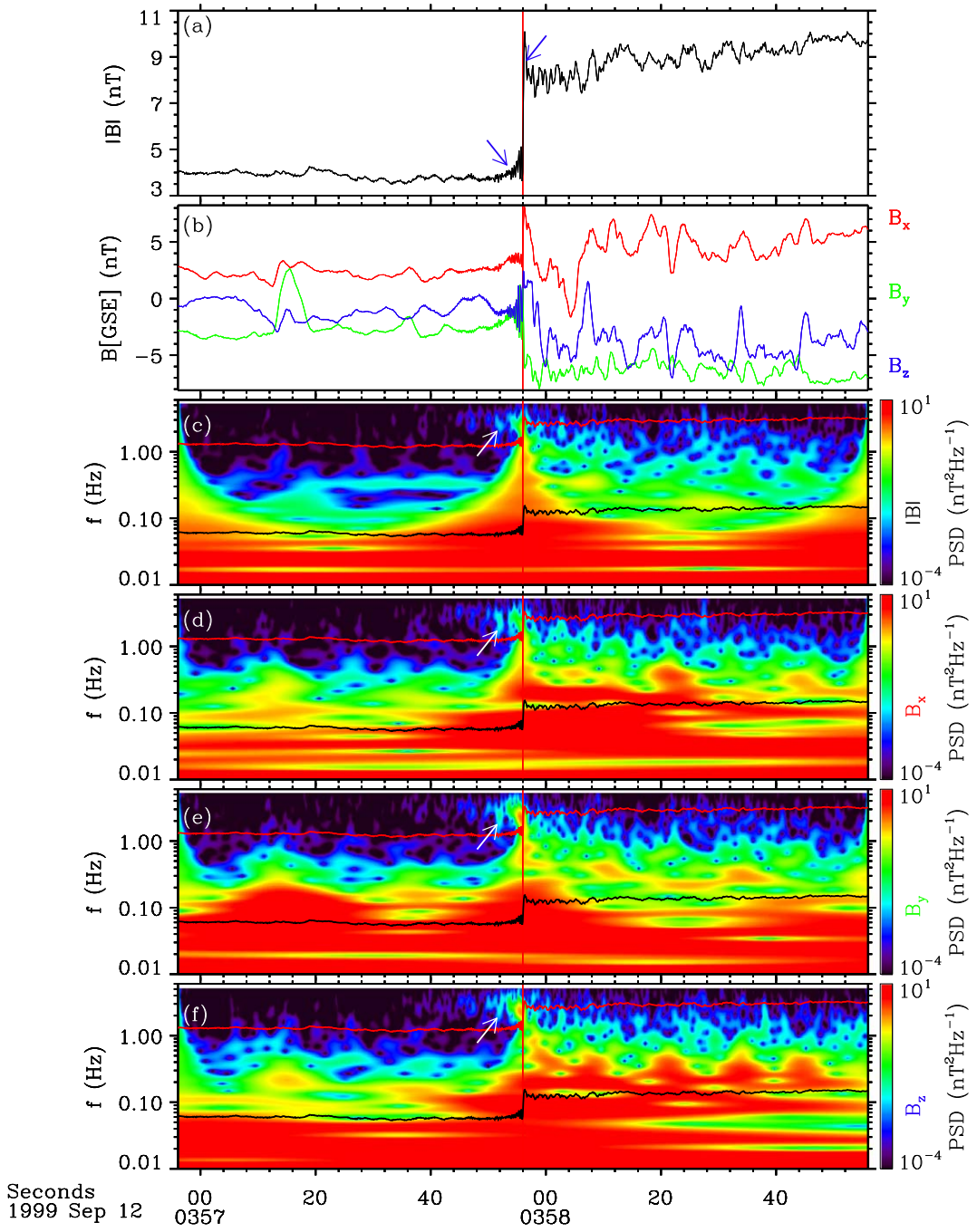


Figure 4. Wavelet analysis of the magnetic field measurements around the IP shock. From top to bottom, the panels show the magnetic field magnitude, the GSE components of the magnetic field, the wavelet analysis of the magnetic field magnitude $|B|$, and components including B_x, B_y, and B_z, respectively. The frequency range of the wavelet analysis is from 0.01 to 5.5 Hz. The two blue arrows in panel (a) indicate the foot (left) and overshoot (right) structures. The white arrows in panels (c)–(f) indicate the precursor whistlers. The vertical red line marks the IP shock. In panels (c)–(f), the local proton cyclotron frequency (horizontal black line) and 1/2 lower hybrid frequency (horizontal red line) are plotted for reference.

of $\hat{K}_{\rm GSE}$ due to projection effects, which results from using only single-spacecraft magnetic field measurements (Khrabrov & Sonnerup 1998; Wilson et al. 2017). Since $\theta_{\rm kB} > 0°$, the whistlers observed around the shock are oblique whistler waves. The shock angle $\theta_{\rm kn} > 0°$, so they are not likely to be phase standing (Mellott & Greenstadt 1984).

Precursor whistlers are generated through dispersive radiation from the shock ramp or indirectly due to instabilities that are excited by reflected particles (see Wilson et al. 2012, 2017, and references therein). In addition, precursor whistlers can be generated (and/or enhanced) by whistler heat flux instabilities and/or whistler anisotropy instabilities (Wilson et al. 2009; Liu et al. 2018), which are discussed below. Gary et al. (1999) demonstrated that the heat-flux-driven whistler mode is always unstable when the temperature anisotropy of halo electrons $T_{\perp h}/T_{\parallel h} > 1.01$ and always stable when the parallel beta of core electrons $\beta_{\parallel c} \leqslant 0.25$. The primary influence of whistler heat flux instabilities is to pitch-angle-scatter halo electrons through cyclotron resonance. Table 1 shows the electron parameters derived from the 3DP/EESA-Low data around the

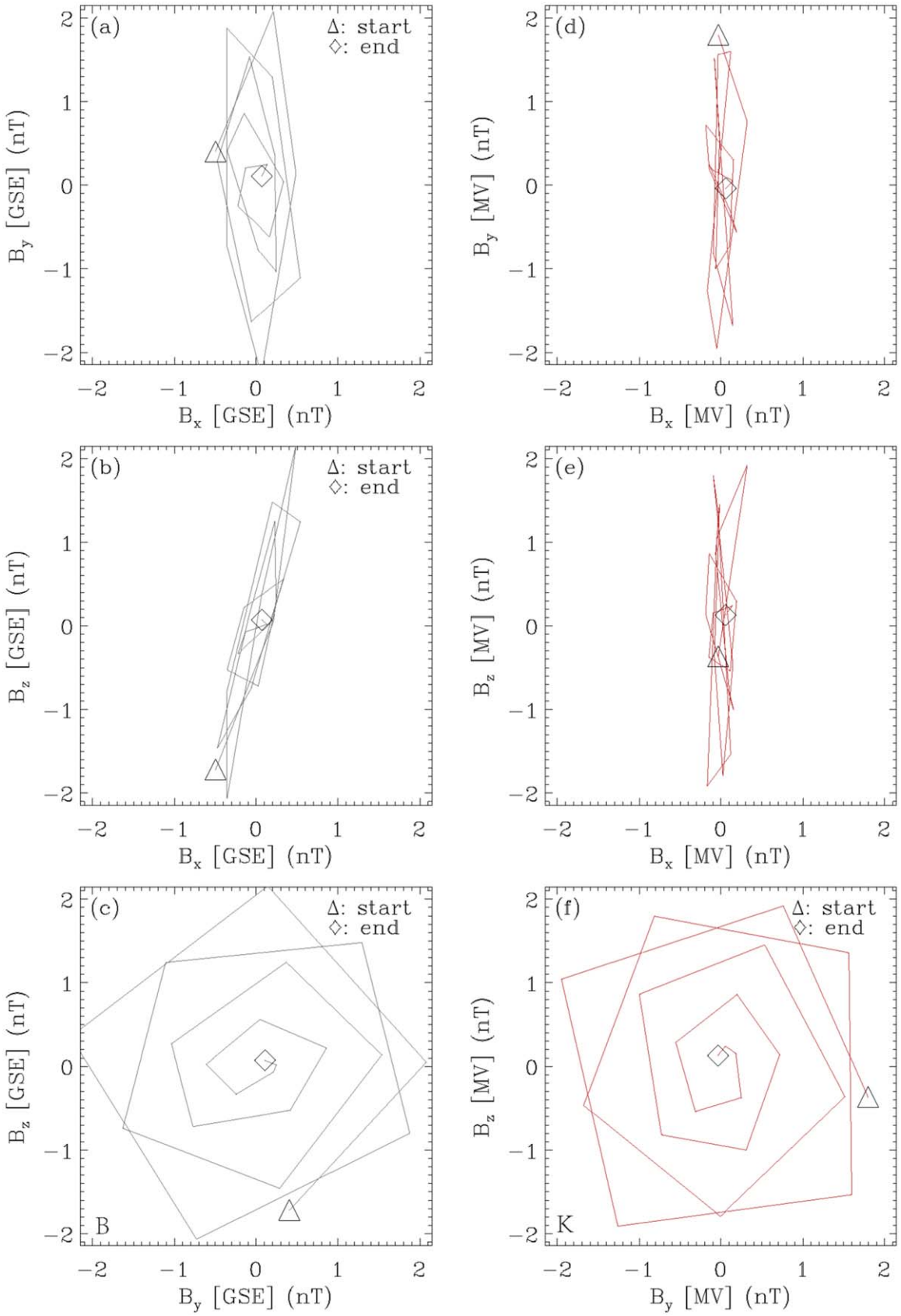


Figure 5. An example of an MV analysis of the waves during the time period of 03:57:55 UT ∼ 03:57:57 UT (2.0 Hz $< f <$ 4.0 Hz in the spacecraft frame, ratio of the intermediate to minimum eigenvalues $\lambda_2/\lambda_3 = 59.71$, and ratio of the maximum to intermediate eigenvalues $\lambda_1/\lambda_2 = 1.110$, $\hat{K}_{\rm GSE} = [0.96715, 0.06149, -0.24665]$, $\theta_{kB} = 53.^{\circ}7$ (or $126.^{\circ}3$), $\theta_{kn} = 14.^{\circ}2$ (or $165.^{\circ}8$), $\theta_{kV} = 12.^{\circ}4$ (or $167.^{\circ}6$)). The hodograms in GSE and MV coordinates are shown. The [*X, Y, Z*]-MV coordinates represent the directions parallel to the minimum, intermediate, and maximum variance eigenvectors, respectively. The projections of the magnetic field (B) and wavevector (K) point outward.

Table 1
Wind/3DP Electron Parameters from EESA-Low Burst Mode Data

Time(UT)	$T_{\perp c}/T_{\parallel c}$	$T_{\perp h}/T_{\parallel h}$	$T_{\parallel h}/T_{\parallel c}$	$\beta_{\parallel c}$	$n_{ce}(cm^{-3})$	$n_{he}(cm^{-3})$	n_{he}/n_{ce}
03:57:49–03:57:52	0.71	0.65	9.85	1.61	3.61	0.27	0.075
03:57:52–03:57:55	0.72	0.89	6.90	1.67	2.27	0.20	0.087
03:57:55–03:57:58	1.10	1.09	7.56	0.84	4.27	0.27	0.063
03:57:58–03:58:02	1.03	1.10	10.31	1.10	7.35	0.10	0.014
03:58:02–03:58:05	0.98	1.07	10.31	1.23	7.20	0.10	0.015

IP shock. Electron parameters were derived by fitting core electrons to bi-Maxwellian distributions and halo electrons to bi-Kappa distributions (Mace & Sydora 2010). For more details about the fitting algorithm, we refer to Wilson et al. (2009) and Liu et al. (2018). From 03:57:55 UT to 03:58:05 UT, whistler heat flux instabilities can be excited, which is a possible driver of the whistler waves. In Table 1, a clear increase in $T_{\perp h}/T_{\parallel h}$ is seen across the shock (03:57:5503:57:58 UT), which may result from the normal cyclotron resonance that can increase the transverse energy of the suprathermal electrons and the normal betatron acceleration of electrons mentioned above. These results illustrate that (when passing through the IP shock) whistler heat flux instabilities may contribute to the increase in perpendicular suprathermal number flux and energy flux (see Figure 3) through pitch-angle scattering together with the normal betatron acceleration of electrons.

2.3. Interactions between IP Shock and Alfvén Waves/Fluctuations

Figure 6 presents the in situ solar wind observations around the IP shock from Wind, including the magnetic field and the plasma measurements. Figures 6(b)–(d) show that the magnetic field components are in phase with the proton bulk velocity components, indicating signatures of Alfvén waves/fluctuations both upstream and downstream of the IP shock. This means that the IP shock is interacting with the ambient Alfvén waves/fluctuations. We further analyze the features of Alfvén fluctuations with the corresponding compressibility C_p (Figure 6(g)), and cross helicity σ_c (Figure 6(h)). The compressibility C_p is defined as $C_p(t) = \frac{\langle \delta N_p^2 \rangle}{\overline{N_p}^2} \frac{\overline{B}^2}{\langle \delta \boldsymbol{B} \cdot \delta \boldsymbol{B} \rangle}$ (Gary 1986; Yao et al. 2013; Zhao et al. 2021a), where $\overline{N_p}$ is the mean proton density, $\overline{B}$ is the mean magnetic field magnitude, δN_p is the fluctuation of the ambient proton density, and $\delta \boldsymbol{B}$ is the ambient magnetic field fluctuation. The cross helicity σ_c is defined as $\sigma_c(t) = \frac{2\langle \delta \boldsymbol{V} \cdot \delta \boldsymbol{V}_A \rangle}{\langle \delta \boldsymbol{V}^2 + \delta \boldsymbol{V}_A^2 \rangle}$ (Matthaeus & Goldstein 1982; Yao et al. 2013), where $\delta \boldsymbol{V}$ is the proton bulk velocity fluctuation and $\delta \boldsymbol{V}_A$ is the fluctuation of the ambient Alfvén velocity. Following similar procedures to those of Yao et al. (2013), we used a moving-time window width of 10 minutes to calculate the background quantities (mean values) and then the corresponding fluctuating quantities. Also, a moving-time step of 3 s was used for the calculations, so that C_p and σ_c were obtained for each 3 s time interval.

Upstream of the IP shock, for most of the time, σ_c is close to one, whereas C_p is close to zero, which indicates signatures of shear Alfvén waves. Since $\sigma_c > 0$ and the ambient magnetic field is in general sunward, the detected Alfvén waves purely propagate antisunward. Also, Figure 6(f) shows that the upstream plasma ($\frac{T_{p\perp}}{T_{p\parallel}} \sim 1.0$) inhibits ion mirror-mode and cyclotron instabilities. Downstream of the IP shock, (1) the IP shock shows evidence for preferentially perpendicular ion heating by the enhanced $T_{p\perp}/T_{p\parallel}$ across the shock, so that the $T_{p\perp}/T_{p\parallel}$ values touch the threshold values of both the ion cyclotron and mirror-mode instabilities. Although the threshold values of the ion cyclotron instabilities are lower than the corresponding values of the ion mirror-mode instabilities, the presence of heavy ions in the solar wind ($n_\alpha/n_p \approx 5\%$ or even larger; see Figure 6(g)) should depress the ion cyclotron wave growth rate, which favors the mirror-mode growth (Price et al. 1986; Liu et al. 2006). Therefore, the shocked plasma downstream of the IP shock is marginally unstable to the mirror mode. (2) Especially, the fluctuations denoted by the region between the two dashed vertical blue lines show mirror-mode features, which is evidenced by the anticorrelated density and magnetic field magnitude fluctuations (Figure 6(a); Hubert et al. 1989; Liu et al. 2006; Zhao et al. 2019a) and the temperature anisotropy exceeding the mirror-mode onset condition (Figure 6(f)). Also, C_p is enhanced in the denoted large-scale structures than in the ambient plasma. (3) Meanwhile, downstream of the IP shock, σ_c has both positive and negative values, and the ambient magnetic field is still generally sunward. Therefore, Alfvén waves in the shocked plasma can be separated into two parts, one propagating sunward ($\sigma_c < 0$), and the other propagating antisunward ($\sigma_c > 0$), which gives direct observational evidence for the simulation results (e.g., Lu et al. 2009). This gives a similar picture that Alfvén waves striking the terrestrial bow shock should launch various disturbances into the magnetosheath, including both antisunward and sunward Alfvén fluctuations (e.g., Sibeck et al. 1997; Cable & Lin 1998; Matsuoka et al. 2000). Furthermore, σ_c varies from positive to negative in the denoted large-scale structures, which indicates that the sunward Alfvén waves may result from the interaction between the antisunward Alfvén waves and mirror-mode waves. This is similar to the process that the antisunward Alfvén waves interacting with the fast and/or slow magnetosonic waves contributes to the growth of the sunward Alfvén waves (e.g., Schwartz 1977; Lacombe & Mangeney 1980).

We checked the ion distribution functions (Figure 7) from the PESA-High instrument on board Wind/3DP to examine the ion dynamics at/around the IP shock interacting with Alfvén waves/fluctuations. The particle distributions have already been transformed into the solar wind bulk flow rest frame based on the proton bulk flow velocities measured by the PESA-Low/3DP instrument. The PESA particle detectors on board the Wind/3DP suite were designed to make measurements of three-dimensional low-energy (<30 keV) ion distributions (Lin et al. 1995). The PESA-Low instrument measures ions from as low as 100 eV to as high as 10 keV with 14 different energy channels, which is designed primarily to provide solar wind bulk properties (i.e., ion density, velocity, and temperature). The PESA-High instrument measures ions of 80 eV–30 keV at 15 different energies. The proton bulk velocity measurements by PESA-Low/3DP agree well with those determined by Wind/SWE Faraday Cups (Ogilvie et al. 1995). As shown in

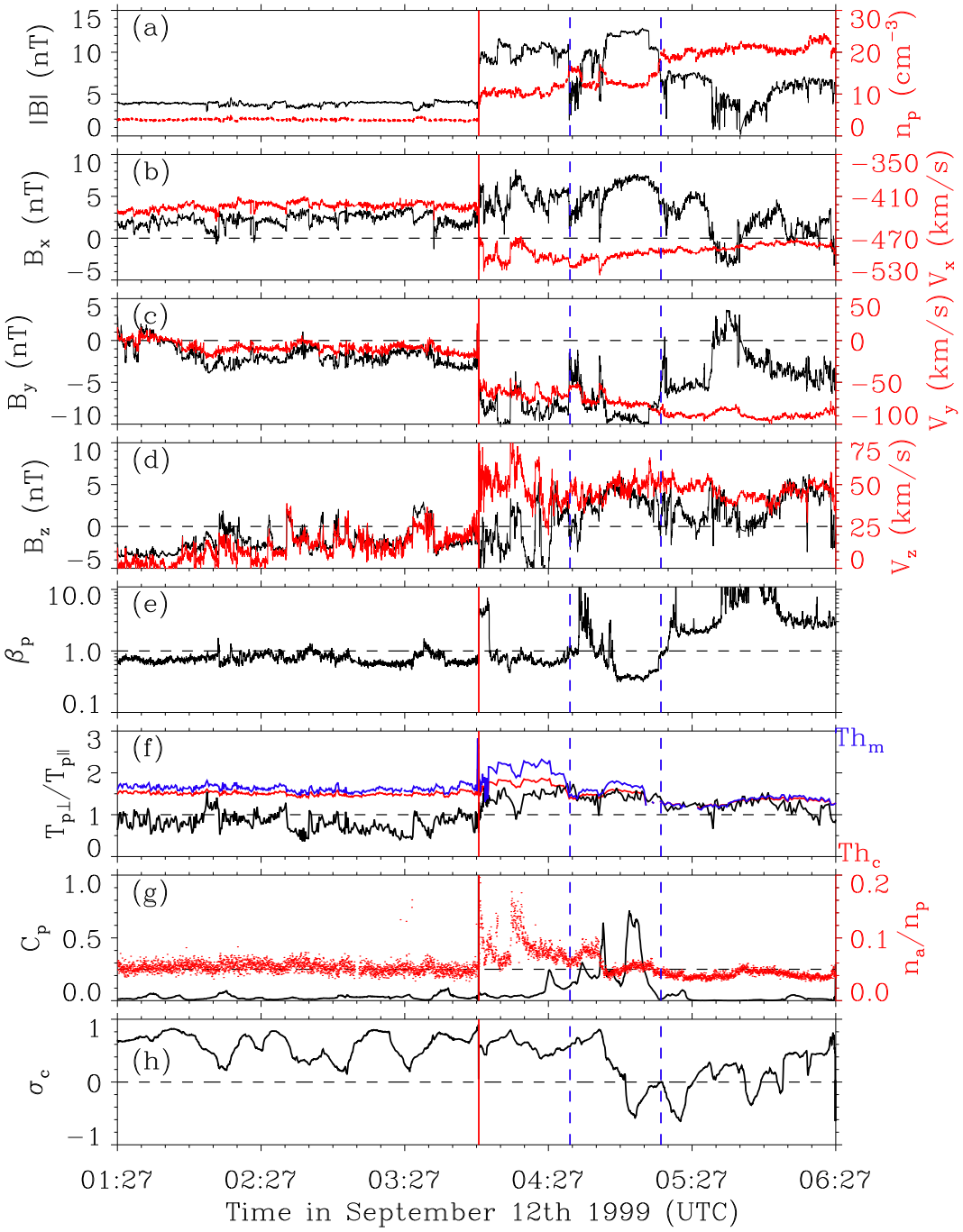


Figure 6. From top to bottom, the panels show (a) the comparison between the magnetic field strength and the proton number density, (b)–(d) the comparison between *X* (*Y, Z*) component of magnetic field and proton bulk velocity in the GSE coordinate, (e) the proton plasma β_p, (f) the proton temperature anistropy (black) with thresholds of ion cyclotron (red) and mirror-mode (blue) instabilities for comparison, (g) the compressibility (black) and alpha abundance (red), and (h) the cross helicity, respectively. The vertical red line marks the IP shock propagating in the terrestrial foreshock region. The region denoted by the two dashed vertical blue lines downstream of the IP shock shows mirror-mode features. For the calculations of thresholds of ion cyclotron and mirror-mode instabilities, we refer to Liu et al. (2006) and references therein.

Figure 7(c), quite intense beam-like populations of gyrating ions (indicated by black arrows) are observed around the shock ramp, with velocities of about 450 km s^{-1}. The observed velocities of the gyrating ions are consistent with the theoretical values according to specular reflection theory (Gosling et al. 1982). The time range of Figure 7(c) covers part of the shock foot/precursor, ramp, and the overshoot structure (Figure 7(a)). The gyrating ions are observed in association with the magnetic foot and overshoot structure, consistent with previous theories/simulations (e.g., Paschmann et al. 1980; Leroy et al. 1982) and observations (e.g., Paschmann et al. 1982; Sckopke et al. 1983; Thomsen et al. 1985). Similarly, Figure 7(d) gives evidence of gyrating ions behind the overshoot of the IP shock (indicated by black arrows). The velocity/density of the gyrating ions behind the overshoot of the IP shock is higher/lower than the corresponding values at the shock ramp. This is similar to the ion dynamics of the IP shock propagating inside an ICME (Liu et al. 2018) and in the ambient solar wind (Wilson et al. 2012).

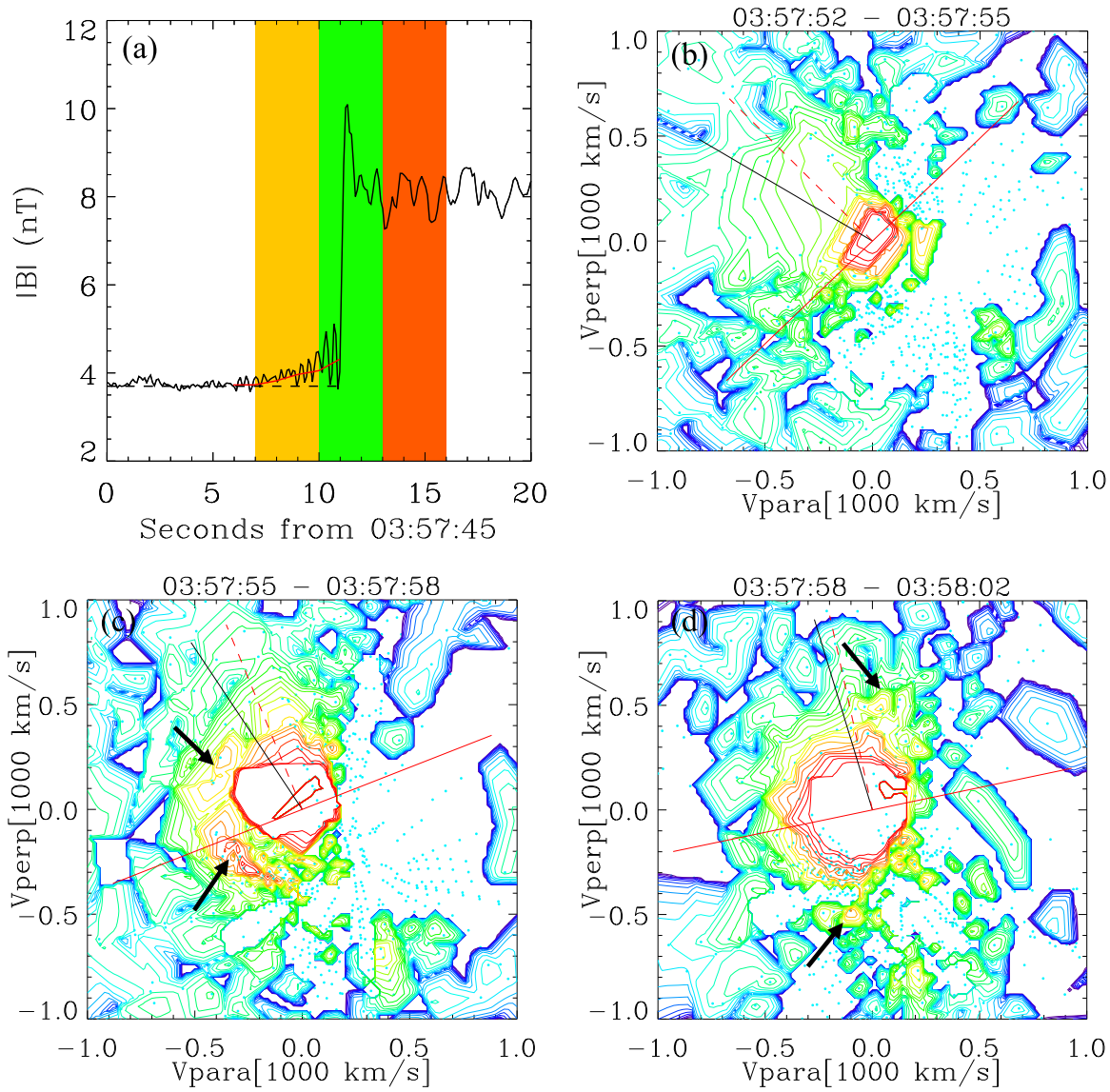


Figure 7. Evolution of the ion distributions (in the solar wind frame) across the shock ramp obtained from the PESA-High/3DP instrument. The solar wind bulk flow velocities, which are used to transform particle distributions into the bulk flow rest frame, were determined from the measurements by the PESA-Low/3DP instrument. (a) Plot of a 20 s window of the magnetic field magnitude (11 samples s^{-1}) around the IP shock. Foot-like magnetic enhancement (red curve) associated with precusor whistlers and magnetic overshoot can be clearly identified near the shock ramp. (b)–(d) Ion distributions corresponding to the time ranges of three color-coded shaded regions in panel (a). The contours show constant phase space density in the plane containing the ambient magnetic field (horizontal axis) and the local solar wind velocity. Projected onto the planes are the shock normal direction (dashed red line), the shock surface (solid red line), and the solar wind velocity direction (solid black line). Gyrating ions are indicated by the black arrows.

Compared to another IP shock in the ambient solar wind ($M_f \sim 4.7$, $\theta_{\rm Bn} = 82°$; see Wilson et al. 2012), the current IP shock ($M_f \sim 2.1$, $\theta_{\rm Bn} = 80°$), which propagates within the terrestrial foreshock, is weaker but associated with more intense beam-like gyrating-reflected ions (Figure 7(c)).

3. Summary and Discussions

This paper reports a comprehensive analysis of the properties of an IP shock magnetically connected to the terrestrial bow shock. Key findings are obtained concerning how the IP shock modifies the terrestrial foreshock.

1. As expected, intense Langmuir waves and $2f_{\rm pe}$ emissions are generally detected when the terrestrial foreshock electron beams are observed. It is quite striking that intensive bursty Langmuir waves are detected downstream of the IP shock. They are likely driven by terrestrial foreshock electron beams penetrating the IP shock. Also, bursty Langmuir waves detected downstream of the IP shock are even more intensive than those upstream of the IP shock. Based on the statistics on the waves at/around the IP shocks, Wilson et al. (2007) showed that Langmuir waves frequently occur in the ramp region, whereas they are rarely detected downstream of the IP shocks. Our results indicate that Langmuir waves excited downstream of the IP shock depend on both the ambient upstream plasma (i.e., transient electron beams penetrating the IP shock) and the IP shock itself. We find that the intensity of the detected Langmuir waves is closely related to the energy of the electron beam and the corresponding ratio of the parallel to perpendicular electron flux. Across the IP shock, the energy of the dominant electron beam is higher

and the corresponding ratio of the parallel to perpendicular electron flux is enhanced, which coincides with the more intensive Langmuir waves.

2. Oblique precursor whistlers are observed around the IP shock, associated with the whistler heat flux instabilities. Whistler heat flux instabilities contribute to the pitch-angle scattering of the suprathermal electrons (both the terrestrial foreshock electrons and strahl electrons from the Sun), together with the normal betatron acceleration that occurs across the shock. This is similar to the picture of the disappearance of bidirectional electrons downstream of an IP shock inside an ICME (Liu et al. 2018).
3. The IP shock is interacting with the Alfvén waves/fluctuations detected in the terrestrial foreshock region. Upstream of the IP shock, Alfvén waves/fluctuations are incompressible and purely propagate antisunward. In contrast, downstream of the IP shock, the shocked plasma shows both Alfvénic and mirror-mode features. Alfvén waves/fluctuations are separated into two parts, one part that propagates sunward, and the other that propagates antisunward, which may be due to the interaction between the Alfvén waves/fluctuations and the mirror-mode waves.
4. Specularly reflected gyrating ions are detected based on the particle distribution, which covers the magnetic foot, ramp, and overshoot structures. This is consistent with the specular reflection theory prediction, and provides evidence that the reflected ions may provide energy dissipation for a supercritical quasi-perpendicular IP Shock (Paschmann et al. 1980; Leroy et al. 1982). We note that more intense beam-like gyrating-reflected ions are associated with the present IP shock ($M_f \sim 2.1$, $\theta_{\rm Bn} = 80°$), compared to those reflected by another IP shock in the ambient solar wind ($M_f \sim 4.7$, $\theta_{\rm Bn} = 82°$; see Wilson et al. 2012). This may be partly explained by the interaction between the IP shock and the upstream Alfvén waves/fluctuations (present within the terrestrial foreshock region), which can generate some rippling at the IP shock front (e.g., Lu et al. 2009). This additional rippling can modify the dynamics of the gyrating ions reflected by the IP shock and lead to some diffusion. A detailed analysis of this interaction requires further investigation.

In summary, this work provides deeper insights into how an IP shock modifies the terrestrial foreshock region via wave analysis and particle distributions. Recent observations from the Parker Solar Probe (Fox et al. 2016) show that the pristine solar wind in the inner heliosphere is highly Alfvénic (e.g., Kasper et al. 2019; Bale et al. 2019; Huang et al. 2020; Zhao et al. 2021a). Also, very many Langmuir waves were detected in the free pristine solar wind (e.g., Bale et al. 2019; Jagarlamudi et al. 2021), which indicates the presence of the transient electron beams near the Sun. The Sun has become more and more active since 2021, and more IP shocks driven by solar eruptions are expected to be observed in the inner heliosphere. The IP shocks near the Sun will interact with Alfvén waves/fluctuations and the transient electron beams in the free pristine solar wind. Therefore, present results may also provide some hints on the properties of IP shocks interacting with Alfvén waves/fluctuations and transient electron beams near the Sun.

M.L. acknowledges Milan Maksimovic, Karl-Ludwig Klein, and Carine Briand for helpful discussions. The research was supported by the CNES and DIM ACAV+ PhD funding in France. Z.Y. was supported by the project of Civil Aerospace "13th Five Year Plan" Preliminary Research in Space Science (Nos. D020301 and D030202) and NSFC under grants 42274210 and 42188101. Y.D.L. was supported by NSFC under grants 41774179 and 42274201, the Specialized Research Fund for State Key Laboratories of China, the CAS Strategic Priority Program on Space Science (XDA15018500), and National Key R&D Program of China (No. 2021YFA0718600). We acknowledge the use of data from Wind/MFI (https://spdf.gsfc.nasa.gov/pub/data/wind/mfi/) and Wind/3DP (http://sprg.ssl.berkeley.edu/wind3dp/). The authors acknowledge CNES (Centre National d'Etudes Spatiales), CNRS (Centre National de la Recherche Scientifique), and Observatoire de Paris for support to the Wind/WAVES team and the CDPP (Centre de Données de la Physique des Plasmas) for the provision of the Wind/WAVES data.

Appendix A
Source of the Transient Electron Beam

In Section 2.1, Figures 2(b)–(e) show that the transient electron flux enhancements around the IP shock mainly come from the direction parallel to the ambient magnetic field. In this context, the ambient magnetic field is in general directed sunward, therefore the parallel electron flux enhancements should come from the terrestrial bow shock. However, the ambient magnetic field rotates slightly, which may change the situation. In Figure 8, we compare the parallel (antiparallel) electron flux with the sunward (antisunward) electron flux. The sunward electron flux is calculated based on the similar technique to calculate the electron PADs. When calculating the parallel (and/or antiparallel) electron flux, the ambient magnetic field vectors are used to calculate the electron pitch angles. In contrast, the sunward unit vector [1, 0, 0] in the GSE coordinate is used to calculate the proxy electron pitch angles and then the sunward (antisunward) electron flux.

Specifically, both Figures 2(b)–(e) and Figure 8 present the measurements derived by the EESA-Low/3DP instrument (Lin et al. 1995). The EESA particle detectors on board the Wind/3DP were designed to make measurements of three-dimensional low-energy (<30 keV) electron distributions. The EESA-Low analyzer covers the energy range from 3 eV to 1.1 keV, whereas the EESA-High analyzer detects electrons of 300 eV to 30 keV. Both instruments have operational fields of view of $180° \times 14°$ and 15 logarithmically spaced energy channels. Each detector sweeps out $4 \times \pi$ steradians in space to give a full distribution in one spacecraft spin (with the spin period being 3 s). The data are combined on board with 88 angular bins for both instruments.

We note that all particle data shown herein have been transformed from the spacecraft into the solar wind bulk flow rest reference frame using the proton bulk velocities measured by the PESA-Low/3DP instrument. For each energy bin, eight pitch-angle (or the proxy ones) bins are defined to calculate the resulting distributions. For example, the mean values of eight defined pitch-angle bins are [14°, 35°, 57°, 79°, 101°, 123°, 145°, and 165°]. The derived distributions are summed and then averaged over each two consecutive defined pitch-angle bins. As a result, the parallel direction covers 14°–35°, the perpendicular direction covers 79°–101°,

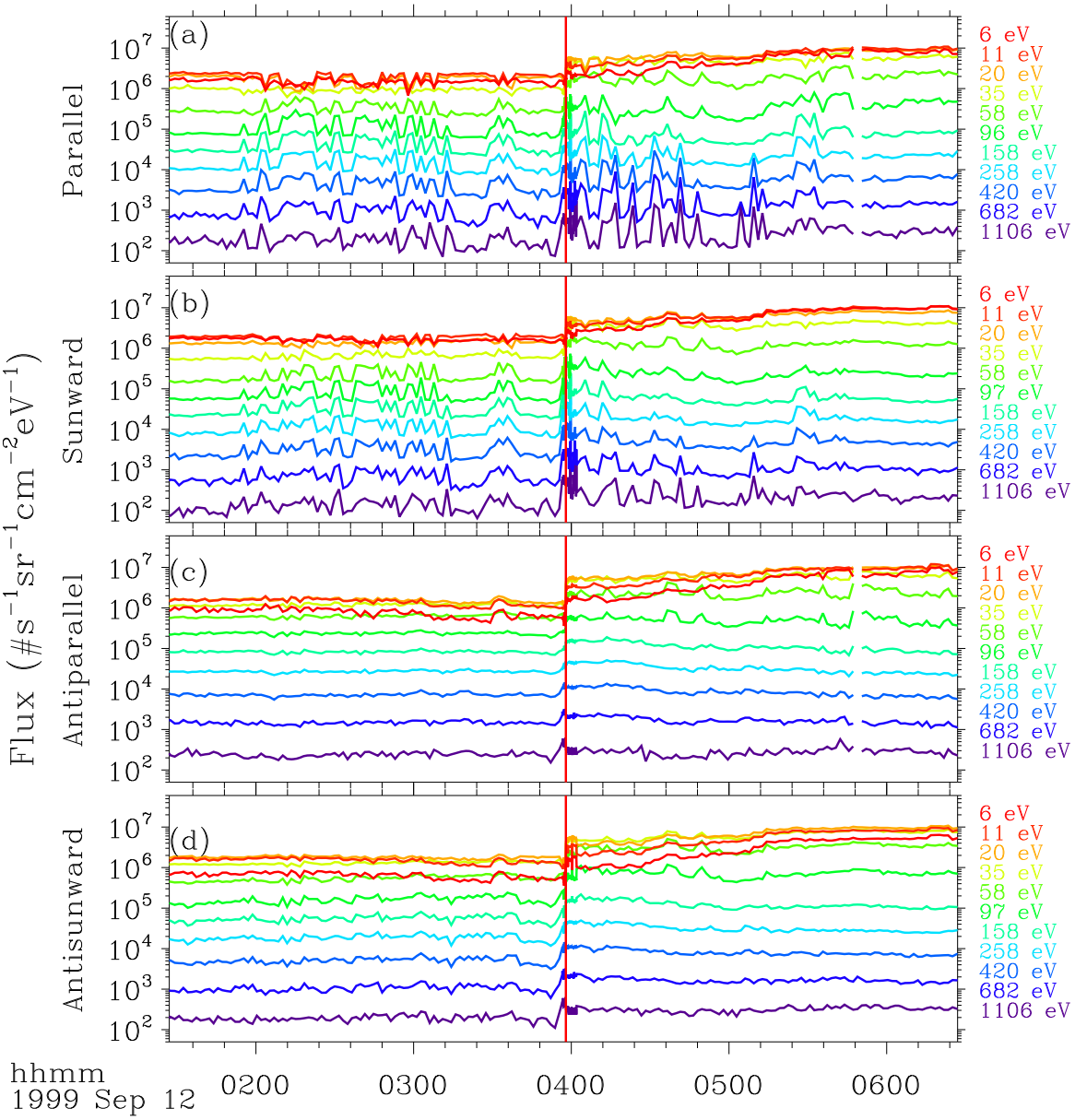


Figure 8. Five-hour expanded view of electron flux measurements from the EESA-Low instrument on board Wind/3DP around the IP shock. From top to bottom, the panels show electron flux (from about 6to 1106 eV) in parallel, sunward, antiparallel, and antisunward directions, respectively. The labeled energies have been corrected by considering the spacecraft potential. The vertical red line marks the time when the IP shock was detected.

and the antiparallel direction covers 145°–165°. The sunward and antisunward electron flux are defined in a similar way. Moreover, the EESA-Low measurements have been corrected by considering the effects of the spacecraft floating potential. We estimate the spacecraft potential following the previous methods/procedures outlined in Salem et al. (2001). Only measurements from the energy channels higher than the estimated spacecraft potential are shown. The labeled energies are the mean values of the corresponding energy channels after correcting the estimated spacecraft potential. Figures 8(a)–(b) show a clear concurrence of the parallel electron flux enhancements and the sunward electron flux enhancements. Also, both the antiparallel and antisunward electron flux are relatively quiet (see Figures 8(c)–(d)). Therefore, we confirm that the transient parallel electron flux enhancements should exclusively come from the terrestrial bow shock.

Appendix B
Exclusion of IP Shock as a Source

Previous investigations (e.g., Bale et al. 1999; Pulupa & Bale 2008) showed that the foreshock electrons of a quasi-perpendicular IP shock can cause increases in both the parallel and antiparallel electron flux in front of the shock surface. Furthermore, the timespan of such an IP electron foreshock region observed by the spacecraft is usually shorter than one minute. Therefore, such IP foreshock electrons likely do not contribute to the transient electron flux enhancements mentioned in Appendix A. IP foreshock electrons may nevertheless affect the analysis in Section 2.2. As a result, we need to verify whether Wind detected such IP foreshock electrons. Based on the burst-mode particle data set, Figure 9 shows that no apparent increases are observed in electron flux in either the parallel (sunward) or antiparallel (antisunward) directions

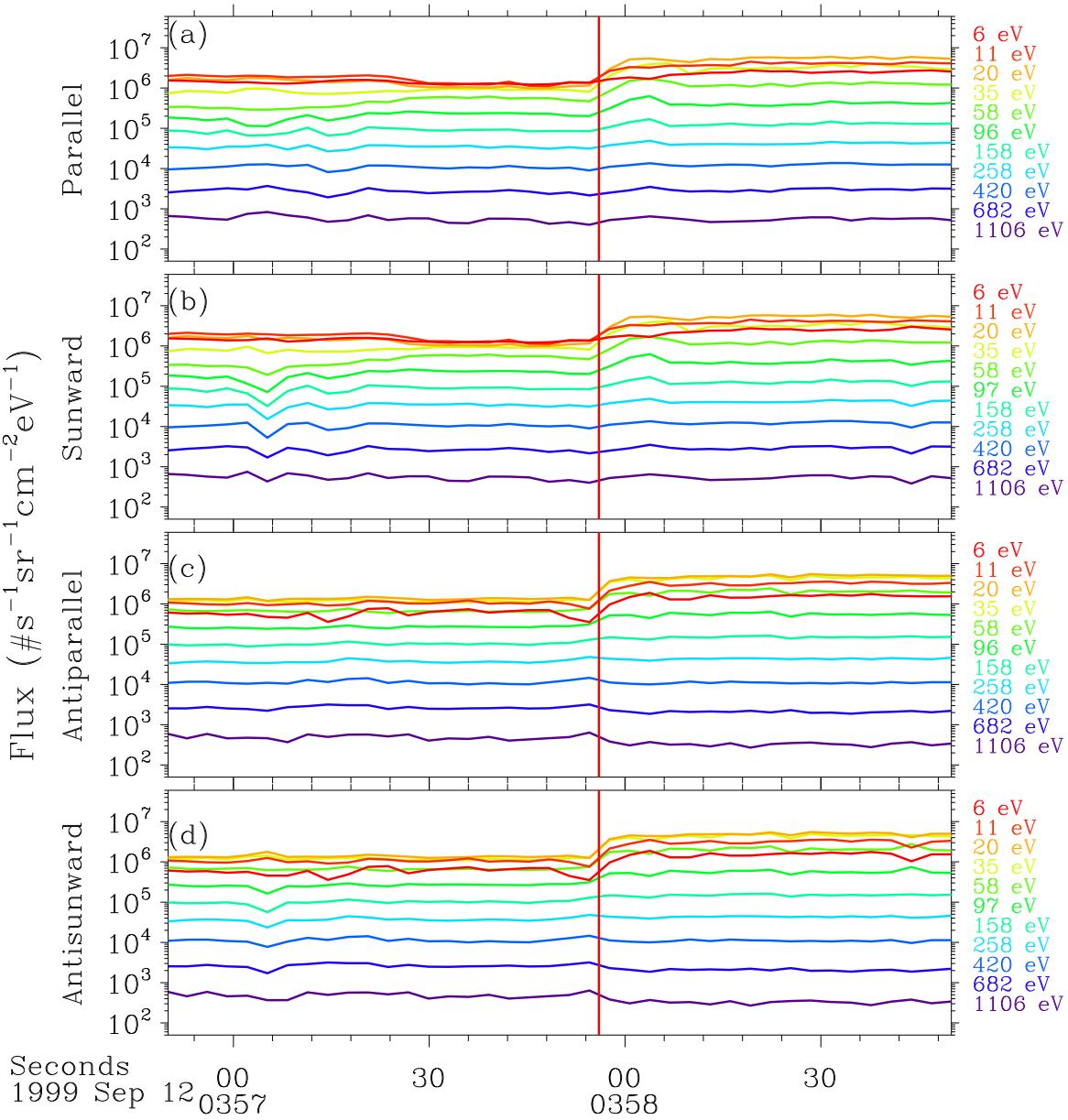


Figure 9. Same as Figure 8, but for a 2-minute expanded view of electron flux measurements around the IP shock. Note that only the burst-mode particle data set is considered in this plot.

upstream of the IP shock. Therefore, we conclude that the IP foreshock electrons likely did not pass Wind.

ORCID iDs

Mingzhe Liu https://orcid.org/0000-0003-2981-0544
Zhongwei Yang https://orcid.org/0000-0002-1509-1529
Ying D. Liu https://orcid.org/0000-0002-3483-5909
Bertrand Lembége https://orcid.org/0000-0002-5528-0228
Karine Issautier https://orcid.org/0000-0002-2757-101X
L. B. Wilson III https://orcid.org/0000-0002-4313-1970
Siqi Zhao https://orcid.org/0000-0003-4268-7763
Vamsee Krishna Jagarlamudi https://orcid.org/0000-0002-4313-1970
Xiaowei Zhao https://orcid.org/0000-0002-4016-5710
Jia Huang https://orcid.org/0000-0002-9954-4707
Nicolina Chrysaphi https://orcid.org/0000-0002-4389-5540

References

Bale, S. D., Badman, S. T., Bonnell, J. W., et al. 2019, Natur, 576, 237
Bale, S. D., Larson, D. E., Lin, R. P., et al. 2000, JGR, 105, 27353
Bale, S. D., Reiner, M. J., Bougeret, J. L., et al. 1999, GeoRL, 26, 1573
Bougeret, J. L., Kaiser, M. L., Kellogg, P. J., et al. 1995, SSRv, 71, 231
Cable, S., & Lin, Y. 1998, GeoRL, 25, 1821
Fox, N. J., Velli, M. C., Bale, S. D., et al. 2016, SSRv, 204, 7
Gary, S. P. 1986, JPlPh, 35, 431
Gary, S. P., Skoug, R. M., & Daughton, W. 1999, PhPl, 6, 2607
Goncharov, O., Koval, A. Å., Afránková, J., et al. 2018, JGRA, 123, 3822
Gosling, J. T., Baker, D. N., Bame, S. J., et al. 1987, JGR, 92, 8519
Gosling, J. T., Thomsen, M. F., Bame, S. J., et al. 1982, GeoRL, 9, 1333
Grognard, R. J. M. 1975, AuJPh, 28, 731
Hoang, S., Lacombe, C., MacDowall, R. J., & Thejappa, G. 2007, JGRA, 112, A09102
Huang, J., Kasper, J. C., Stevens, M., et al. 2020, arXiv:2005.12372
Hubert, D., Perche, C., Harvey, C. C., Lacombe, C., & Russell, C. T. 1989, GeoRL, 16, 159
Issautier, K., Perche, C., Hoang, S., et al. 2005, AdSpR, 35, 2141

Jagarlamudi, V. K., Dudok de Wit, T., Froment, C., et al. 2021, A&A, 650, A9
Kasaba, Y., Matsumoto, H., Omura, Y., et al. 2000, JGR, 105, 79
Kasper, J. C., Bale, S. D., Belcher, J. W., et al. 2019, Natur, 576, 228
Khrabrov, A. V., & Sonnerup, B. U. Ö. 1998, JGR, 103, 6641
Lacombe, C., & Mangeney, A. 1980, A&A, 88, 277
Lembege, B., Giacalone, J., Scholer, M., et al. 2004, SSRv, 110, 161
Lembège, B., & Savoini, P. 2002, JGRA, 107, 1037
Lepping, R. P., Acũna, M. H., Burlaga, L. F., et al. 1995, SSRv, 71, 207
Leroy, M. M., Winske, D., Goodrich, C. C., Wu, C. S., & Papadopoulos, K. 1982, JGR, 87, 5081
Lin, R. P., Anderson, K. A., Ashford, S., et al. 1995, SSRv, 71, 125
Liu, M., Liu, Y. D., Yang, Z., Wilson, L. B., III, & Hu, H. 2018, ApJL, 859, L4
Liu, Y., Richardson, J. D., Belcher, J. W., Kasper, J. C., & Skoug, R. M. 2006, JGR, 111, A09108
Liu, Y. D., Luhmann, J. G., Kajdič, P., et al. 2014b, NatCo, 5, 3481
Liu, Y. D., Luhmann, J. G., Möstl, C., et al. 2012, ApJL, 746, L15
Liu, Y. D., Yang, Z., Wang, R., et al. 2014a, ApJL, 793, L41
Lu, Q., Hu, Q., & Zank, G. P. 2009, ApJ, 706, 687
Lugaz, N., Farrugia, C. J., Smith, C. W., & Paulson, K. 2015, JGRA, 120, 2409
Mace, R. L., & Sydora, R. D. 2010, JGR, 115, A07206
Matsumoto, H., Kojima, H., Kasaba, Y., et al. 1997, AdSpR, 20, 683
Matsuoka, A., Southwood, D. J., Kokubun, S., & Mukai, T. 2000, JGR, 105, 18,361
Matthaeus, W. H., & Goldstein, M. L. 1982, JGR, 87, 6011
McKenzie, J. F., & Westphal, K. O. 1969, P&SS, 17, 1029
Mellott, M. M., & Greenstadt, E. W. 1984, JGR, 89, 2151
Meyer-Vernet, N., Issautier, K., & Moncuquet, M. 2017, JGRA, 122, 7925
Meyer-Vernet, N., & Perche, C. 1989, JGR, 94, 2405
Möstl, C., Farrugia, C. J., Kilpua, E. K. J., et al. 2012, ApJ, 758, 10
Ogilvie, K. W., Chornay, D. J., Fritzenreiter, R. J., et al. 1995, SSRv, 71, 55
Parks, G. K., Lee, E., Fu, S. Y., et al. 2017, RvMPP, 1, 1
Paschmann, G., Sckopke, N., Asbridge, J. R., Bame, S. J., & Gosling, J. T. 1980, JGR, 85, 4689
Paschmann, G., Sckopke, N., Bame, S. J., & Gosling, J. T. 1982, GeoRL, 9, 881
Peredo, M., Slavin, J. A., Mazur, E., & Curtis, S. A. 1995, JGR, 100, 7907
Price, C. P., Swift, D. W., & Lee, L. C. 1986, JGR, 91, 101
Pulupa, M., & Bale, S. D. 2008, ApJ, 676, 1330
Pulupa, M., Bale, S. D., Opitz, A., et al. 2012, arXiv:1202.3678
Pulupa, M. P., Bale, S. D., & Salem, C. 2011, GeoRL, 38, L14105
Přech, L., Němeček, Z., & Šafránková, J. 2009, EP&S, 61, 610
Reiner, M. J., Kaiser, M. L., Fainberg, J., Desch, M. D., & Stone, R. G. 1996, GeoRL, 23, 1247
Roelof, E. C., & Sibeck, D. G. 1993, JGR, 98, 21421
Šafránková, J., Němeček, Z., Přech, L., et al. 2007a, P&SS, 55, 2324
Šafránková, J., Němeček, Z., Přech, L., et al. 2007b, JGRA, 112, A08212
Saito, S., & Umeda, T. 2011, ApJ, 736, 35
Salem, C., Bosqued, J. M., Larson, D. E., et al. 2001, JGR, 106, 21701
Savoini, P., & Lembège, B. 2001, JGR, 106, 12975
Savoini, P., & Lembege, B. 2009, AGUFM, SH31A–1470
Schwartz, S. J. 1977, MNRAS, 178, 399
Sckopke, N., Paschmann, G., Bame, S. J., Gosling, J. T., & Russell, C. T. 1983, JGR, 88, 6121
Sibeck, D. G., Takahashi, K., Kokubun, S., et al. 1997, GeoRL, 24, 3133
Thomsen, M. F., Gosling, J. T., Bame, S. J., & Rusell, C. T. 1985, JGR, 90, 267
Vinas, A. F., & Scudder, J. D. 1986, JGR, 91, 39
Wang, X., Tu, C., Wang, L., He, J., & Marsch, E. 2015, GeoRL, 42, 3654
Wilson, L. B. 2016, GMS, 216, 269
Wilson, L. B. I., Brosius, A. L., Gopalswamy, N., et al. 2021, RvGeo, 59, e2020RG000714
Wilson, L. B., III, Cattell, C., Kellogg, P. J., et al. 2007, PhRvL, 99, 041101
Wilson, L. B., III, Cattell, C. A., Kellogg, P. J., et al. 2009, JGRA, 114, A10106
Wilson, L. B., III, Koval, A., Szabo, A., et al. 2012, GeoRL, 39, L08109
Wilson, L. B., III, Koval, A., Szabo, A., et al. 2017, JGRA, 122, 9115
Yang, Z., Lu, Q., Liu, Y. D., & Wang, R. 2018, ApJ, 857, 36
Yang, Z. W., Lembège, B., & Lu, Q. M. 2012, JGRA, 117, A07222
Yao, S., He, J. S., Tu, C. Y., Wang, L. H., & Marsch, E. 2013, ApJ, 774, 59
Yoon, P. H., Wu, C. S., Vinas, A. F., et al. 1994, JGR, 99, 481
Zhao, S. Q., Xiao, C. J., Liu, T. Z., et al. 2021b, JGRA, 126, e28525
Zhao, S. Q., Xiao, C. J., Wang, X. G., et al. 2019a, JGRA, 124, 200
Zhao, S. Q., Yan, H., Liu, T. Z., Liu, M., & Shi, M. 2021a, ApJ, 923, 253
Zhao, X., Liu, Y. D., Hu, H., & Wang, R. 2019b, ApJ, 882, 122